Ab initio molecular orbital model of scanning tunneling microscopy

Taro Fujita, Hiromi Nakai, and Hiroshi Nakatsuji[a)]
Department of Synthetic Chemistry and Biological Chemistry, Faculty of Engineering, Kyoto University, Sakyo-ku, Kyoto, 606-01, Japan

(Received 7 July 1995; accepted 27 October 1995)

An *ab initio* model of scanning tunneling microscopy (STM) is presented in the framework of the perturbation theory of Bardeen. The tip and sample are represented by the cluster model, and the first-order wave functions are calculated by *ab initio* Hartree–Fock (HF), configuration interaction (CI), and symmetry adapted cluster (SAC)/SAC-CI methods. This model was applied to simple tip–sample systems such as Pd_2–Ag_2, Pd_2–C_6H_6, Pd_2–$(C_6H_6)_2$, and Li_2–Li_2. The calculated STM images were related to the HOMO, LUMO, etc. orbital symmetries of the tip–sample systems. The contribution of the Rydberg orbital was examined at different tip–sample distances. Electron correlations were found to modify the behavior of the tunneling transition probability of the Li_2–Li_2 system vs that calculated by the HF method. © *1996 American Institute of Physics.* [S0021-9606(96)02705-3]

I. INTRODUCTION

Scanning tunneling microscopy (STM) has been widely used as a powerful method for analyzing surface states in real-space since its development by Binnig *et al.* about 10 years ago.[1] STM and related technologies constitute an actively growing field. In recent years, STM has been used not only as an analysis method, but also as a tool to manipulate solid surface atoms at the nanometer-scale. Furthermore, new techniques, such as atomic force microscopy (AFM), have been developed. Without question, STM has had a great impact on many fields of material science. However, despite its usefulness, the actual mechanism by which STM can *see* surface atoms is not yet totally understood. An STM image does not necessarily represent the arrangement of the surface atoms, but reflects local electronic structures of the solid surface. Therefore, theoretical analyses, which take the electronic structure of the tip and sample into account, are necessary to interpret the STM image.

Since Tersoff and Hamann attempted to explain the STM images of Au(110) 2×1 and 3×1, and Si(111) 7×7 using their theoretical model,[2] many other theoretical methods for analyzing STM images have been proposed.[2–11] To address electron tunneling, Tersoff and Hamann used Bardeen's perturbative approach[12] by assuming that the tip–sample interaction was very weak and using an *s*-type tip. They concluded that the tunneling current is proportional to the local density of the states of the sample at the Fermi energy level at the center of the curvature of the tip. Furthermore, the size of an *s*-type tip must correspond to the atomic size in order to reproduce the STM image at atomic resolution. Tsukada *et al.*[5–7] modified Tersoff–Hamann's model by considering the effect of the electronic state of the tip, by introducing the LCAO method in the wave functions of both the tip and sample, and performed STM simulations using the density functional method. They showed in their simulation of the graphite surface that one top atom of the tip modeled by W_9–W_{14} is most responsible for the electron current giving the STM image.[7] Ou-Yang *et al.*[11] treated the tip and sample as semi-infinite systems using the tight-binding approach with the Hückel method. These models have been applied to various STM systems.

In this paper, we propose an *ab initio* quantum chemical method of an electron's tunneling probability in STM based on Bardeen's theory. First, we formulated the tunneling transition probability using the Hartree–Fock (HF) method and the electron correlated method. In applications, we adopted metal dimers, Pd_2 and Li_2, as the models of the tips since the top atom of the tip is essential to simulate the STM image.[5–7] The simulations at the HF level were carried out for the Pd_2–Ag_2, Pd_2–C_6H_6, and Pd_2–$(C_6H_6)_2$ systems, in which Pd_2 models the tip and Ag_2, C_6H_6, and $(C_6H_6)_2$ model the samples, and the relations between the STM images and the HF molecular orbitals were clarified. Finally, we examined the effect of the electron correlations on the STM image for the Li_2–Li_2 system.

II. THEORETICAL MODEL

A. Tunneling current in the framework of the perturbation theory of Bardeen

In this section, we review and summarize the perturbation theory constructed by Bardeen[12] to explain the tunneling phenomenon. This theory is the basis of our *ab initio* MO model as well as those of Tsukada *et al.*[5–7] and Ou-Yang *et al.*[11] In Bardeen's approach, the weak interaction between two conductors, corresponding to the tip and sample in STM, is considered a time-dependent perturbation.

The time-dependent Hamiltonian is defined as follows:

$$H(t)=H_S+H_T+H_{ST}\theta(t), \tag{1}$$

where H_S and H_T are the Hamiltonians for the two isolated conductors, H_{ST} is the interaction potential between the two

[a)]Author to whom correspondence should be addressed. Also belongs to the Institute for Fundamental Chemistry, 34-4 Tanaka Nishi-Hiraki-cho, Sakyo-ku, Kyoto, 606, Japan.

 0021-9606/96/104(6)/2410/8/$10.00

conductors, and $\theta(t)$ is a step function which equals zero at $t<0$ and unity at $t>0$. Suffixes S and T represent the tip and sample, respectively.

The tunneling current is determined by the tunneling transition probability from the initial unperturbed state to the final electron-transferred state, which corresponds to the cationic and anionic states of the two conductors. According to Oppenheimer's method,[13] the time-dependent solution, $\Psi(t)$, is a linear combination of the initial state, Ψ_0, and the various final states, $\Psi_{m\to n}$ as follows:

$$\Psi(t)=a(t)\Psi_0 e^{-iE_0 t/\hbar} + \sum_{m',n'} b_{m'\to n'}(t)\Psi_{m'\to n'} e^{-iE_{m'\to n'}t/\hbar}, \tag{2}$$

where E_0 and $E_{m\to n}$ are the energies of the Ψ_0 and $\Psi_{m\to n}$ states, respectively. These energies represent the sum of the energies of the isolated conductors due to noninteraction between them in the unperturbed condition.

Introducing Eq. (2) into the time-dependent Schrödinger equation,

$$H(t)\Psi(t)=i\frac{d}{dt}\Psi(t), \tag{3}$$

we obtain

$$a(t)H(t)\Psi_0 e^{-iE_0 t/\hbar} + \sum_{m',n'} b_{m'\to n'}(t)H(t)\Psi_{m'\to n'} e^{-iE_{m'\to n'}t/\hbar} = i\frac{d}{dt}\left[a(t)\Psi_0 e^{-iE_0 t/\hbar} + \sum_{m',n'} b_{m'\to n'}(t)\Psi_{m'\to n'} e^{-iE_{m'\to n'}t/\hbar}\right]. \tag{4}$$

Multiplying Eq. (4) by $\Psi_{m\to n}$ from the left-hand side, integrating over the entire space, and using the ortho normality of the wave functions, we obtain

$$a(t)\int \Psi_{m\to n} Hst \Psi_0 d\tau e^{-iE_0 t/\hbar} + \sum_{m',n'} b_{m'\to n'}(t) \times \int \Psi_{m\to n} Hst \Psi_{m'\to n'} d\tau e^{-iE_{m'\to n'}t/\hbar} = i\left[a(t)\int \Psi_{m\to n}\Psi_0 d\tau e^{-iE_0 t/\hbar} + b_{m\to n}(t)e^{-iE_{m\to n}t/\hbar}\right]. \tag{5}$$

We assume that, in the initial stage of tunneling, $a(t)$ equals unity and $b_{m'\to n'}$ equals zero. When the overlapping integrals between the initial and final states are neglected, Eq. (5) becomes

$$i\frac{d}{dt}b_{m\to n}(t)=\int \Psi_{m\to n} H_{ST}\Psi_0 d\tau e^{i(E_{m\to n}-E_0)t/\hbar}. \tag{6}$$

After integration using the formula, $\lim_{t\to\infty}(\sin^2 xt)/x^2 t=\pi\delta(x)$, we obtain

$$\begin{aligned} P_{m\to n} &= \lim_{t\to\infty}|b_{m\to n}|^2/t \\ &= \left(\frac{2\pi}{\hbar}\right)\left|\int \Psi_{m\to n} H_{ST}\Psi_0 d\tau\right|^2 \delta(E_0-E_{m\to n}) \\ &= \left(\frac{2\pi}{\hbar}\right)\left|\int \Psi_{m\to n}[H-(H_S+H_T)]\Psi_0 d\tau\right|^2 \times \delta(E_0-E_{m\to n}) \\ &= \left(\frac{2\pi}{\hbar}\right)\left|\int \Psi_{m\to n}[H-(E_S+E_T)]\Psi_0 d\tau\right|^2 \times \delta(E_0-E_{m\to n}) \\ &= \left(\frac{2\pi}{\hbar}\right)\left|\int \Psi_{m\to n} H\Psi_0 d\tau\right|^2 \delta(E_0-E_{m\to n}) \\ &= \left(\frac{2\pi}{\hbar}\right)|M_{m\to n}|^2\delta(E_0-E_{m\to n}), \end{aligned} \tag{7}$$

where $M_{m\to n}$ is called the tunneling matrix element and the delta function appears according to the energy conservation law before and after the tunneling. The tunneling current is obtained by summing the $P_{m\to n}$ of all possible transitions. Only the transitions for which $E_0-E_{m\to n}$ equals zero, which varies with the bias voltage, contribute to the current. This shows that the current is essentially proportional to $|M_{m\to n}|^2$ of the transition which gives a large contribution.

B. Tunneling matrix element used by the HF wave function

In this section, we attempt to calculate the tunneling matrix element, $M_{m\to n}$, using the HF method. First, the initial state, which is the ground state in the unperturbed condition, is represented as the product of the two HF wave functions of the isolated tip and sample as follows:

$$|\Psi_0\rangle = A|\Psi^S\rangle|\Psi^T\rangle = A|\phi_1^S\phi_2^S\cdots\phi_m^S\cdots\phi_{N_S}^S\rangle|\phi_1^T\phi_2^T\cdots\phi_{N_T}^T\rangle, \tag{8}$$

where A is an antisymmetrizing operator, ϕ_i is a spin–orbital, and N_S and N_T are the numbers of electrons of the tip and sample, respectively. The final electron-transferred states are represented on the basis of Koopman's theorem. For example, electron-transfer from the sample to the tip is given by the single excitation from an occupied orbital of the sample ϕ_m, to an unoccupied of the tip, ϕ_n, as follows:

$$|\Psi_{m\to n}^{CT}\rangle = A|\Psi_m^S\rangle|\Psi_n^T\rangle = A|\phi_1^S\phi_2^S\cdots\phi_{m-1}^S\phi_{m+1}^S\cdots\phi_{N_S}^S\rangle|\phi_1^T\phi_2^T\cdots\phi_{N_T}^T\phi_n^T\rangle. \tag{9}$$

Using the wave functions of the initial and final states given by Eqs. (8) and (9), the tunneling matrix element is expressed as

$$M_{m\to n}=\langle\Psi^{CT}_{m\to n}|\hat{H}|\Psi_0\rangle$$
$$=\sqrt{2}\Bigg[\langle\phi^T_n|\hat{h}|\phi^S_m\rangle + \sum_k^{N_S+N_T}\langle\phi^T_n(\phi^S,\phi^T)_k|\phi^S_m(\phi^S,\phi^T)_k\rangle - \sum_k^{N_S+N_T}\langle\phi^T_n(\phi^S,\phi^T)_k|(\phi^S,\phi^T)_k\phi^S_m\rangle\Bigg], \quad (10)$$

where the first term involves only one electron integral and the second and third terms involve two electron integrals. According to the Brillouin theorem, the value of $M_{m\to n}$ becomes zero if the HF wave functions are calculated in the combined system of the two conductors. Since the Brillouin theorem is valid within the sample or the tip, $\langle\Psi^{CT}_{m\to n}|\hat{H}_S+\hat{H}_T|\Psi_0\rangle$ becomes zero and $M_{m\to n}$ represents the magnitude of the perturbative term, $\langle\Psi^{CT}_{m\to n}|\hat{H}_{ST}|\Psi_0\rangle$.

The present method for calculating $M_{m\to n}$ with the volume integral over the entire space is *analytical*, as opposed to previous *numerical* methods[2–6] which use a surface integral. In the approximation of Koopman's excitation, the state-energy difference in Eq. (7) is transformed to the orbital-energy difference as follows:

$$E_0-E_{m\to n}=E^S_0+E^T_0-(E^S_m+E^T_n)=E^S_0-E^S_m+E^T_0-E^T_n$$
$$=\epsilon_m-\epsilon_n. \quad (11)$$

Using Eqs. (10) and (11), the tunneling transition probability is expressed as

$$P_{m\to n}=\left(\frac{2\pi}{\hbar}\right)|M_{m\to n}|^2\delta(E_0-E_{m\to n})$$
$$=\left(\frac{2\pi}{\hbar}\right)\Bigg|\sqrt{2}\Bigg(\langle\phi^T_n|\hat{h}|\phi^S_m\rangle + \sum_k^{N_S+N_T}\langle\phi^T_n(\phi^S,\phi^T)_k|\phi^S_m(\phi^S,\phi^T)_k\rangle - \sum_k^{N_S+N_T}\langle\phi^T_n(\phi^S,\phi^T)_k|(\phi^S,\phi^T)_k\phi^S_m\rangle\Bigg)\Bigg|^2$$
$$\times\delta(\epsilon_m-\epsilon_n), \quad (12)$$

and a representation like that of Tersoff–Hamann becomes possible,[2]

$$I_{T\to S}=\frac{2\pi e}{\hbar}\sum_{mn}|M_{m\to n}|^2 f(\epsilon_n+\mathrm{eV})[1-f(\epsilon_m)]$$
$$\times\delta(\epsilon_n-\epsilon_m+\mathrm{eV}) \quad (13)$$

where f is the Fermi distribution function

$$f(\epsilon)=[e^{(\epsilon-E_F)/kT}+1]^{-1},$$

and eV is the bias voltage between the tip and sample.

C. Tunneling current used by the correlated wave function

The excited states, which appear as the final states in the tunneling current calculations of Sec. II A, are usually strongly influenced by the electron correlation effect. To describe the electronic structures of metals, which comprise the tip and sample in STM, electron correlations are expected to be important even in the ground state. Therefore, the effect of electron correlations on tunneling current calculations should be examined. Since the formulation in Sec. II B is based on the HF method, an extension to the correlated method is straightforward.

We first show the method for calculating the tunneling matrix element using the configuration interaction (CI) wave function. With the CI method, the initial and final states of the tunneling matrix element in Eq. (7) are expressed by

$$|\Psi^{\mathrm{CI}}_0\rangle=\sum_I C^0_I S^+_I|\Psi^{\mathrm{HF}}_0\rangle, \quad (14)$$

$$|\Psi^{\mathrm{CI}}_{m\to n}\rangle=\sum_J C^{m\to n}_J S^+_J|\Psi^{\mathrm{HF}}_0\rangle, \quad (15)$$

where $|\Psi^{\mathrm{HF}}_0\rangle$ is the HF wave function of the unperturbed system defined by Eq. (8), C_I is the CI coefficient, and S^+_I is the excitation operator. Using Eqs. (14) and (15), the tunneling matrix element is obtained from the CI wave functions as

$$M^{\mathrm{CI}}_{m\to n}=\langle\Psi^{\mathrm{CI}}_{m\to n}|H|\Psi^{\mathrm{CI}}_0\rangle$$
$$=\sum_{IJ}C^{m\to n*}_I C^0_J\langle\Psi^{\mathrm{HF}}_0|S_I H S^+_J|\Psi^{\mathrm{HF}}_0\rangle. \quad (16)$$

Although the full CI method gives an exact solution of the Schrödinger equation within a given set of basis functions, truncated CI methods, such as single- and double-excitation (SD)-CI, are often used for practical reasons. However, truncated CI methods do not necessarily give a good description of the excited state. On the other hand, the symmetry adapted cluster (SAC) and SAC-CI methods,[14–16] which have been developed in our laboratory, give reasonable correlation energies of the ground and excited states, respectively. With the SAC/SAC-CI method, the initial and final states in Eq. (7) are given by

$$|\Psi^{\mathrm{SAC}}_0\rangle=\exp\Bigg(\sum_I C^0_I S^+_I\Bigg)|\Psi^{\mathrm{HF}}_0\rangle, \quad (17)$$

$$|\Psi^{\mathrm{SAC}}_{m\to n}\rangle=\sum_k d_k R^+_k\exp\Bigg(\sum_I C^0_I S^+_I\Bigg)|\Psi^{\mathrm{HF}}_0\rangle, \quad (18)$$

where C^0_I and d_k are the SAC and SAC-CI coefficients, respectively, and S^+_I and R^+_k are the symmetry-adapted excitation operators. We can obtain the tunneling matrix element from the SAC/SAC-CI wave functions as follows:

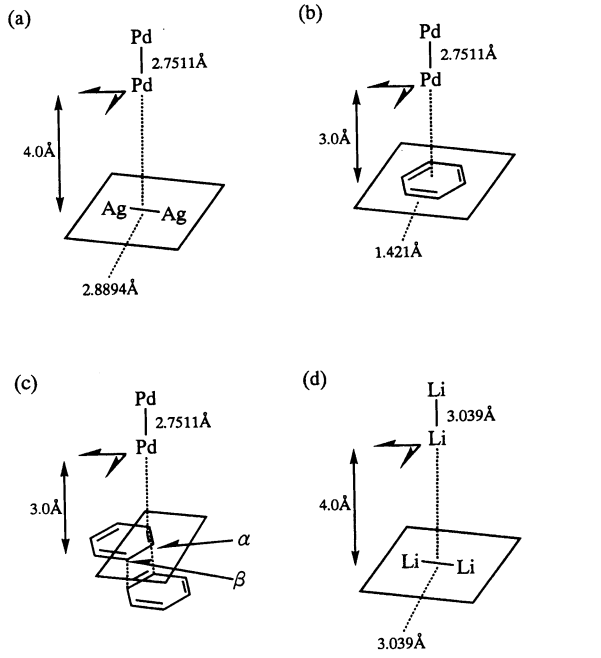

FIG. 1. Geometrical structures of the model clusters used in the simulation of the STM image. (a) Pd_2–Ag_2 system; (b) Pd_2–C_6H_6 system; (c) Pd_2–$(C_6H_6)_2$ system; (d) Li_2–Li_2 system. The tips (Pd_2 and Li_2) are placed perpendicular to the sample surfaces [Ag_2, C_6H_6, and $(C_6H_6)_2$] and the distances between them are kept constant throughout scanning.

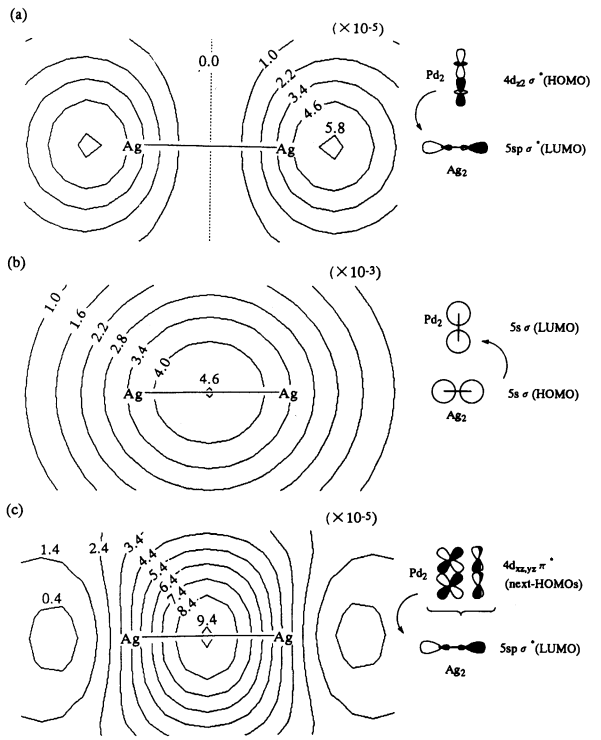

FIG. 2. Theoretical STM images for a Pd_2–Ag_2 system with the geometry shown in Fig. 1(a). The images are drawn as contour maps by plotting the variation of $|M_{m\to n}|^2$ about the tunnelings between two MOs shown below the images. The values of contour lines are shown near the lines.

$$M_{m\to n}^{\mathrm{SAC/SAC\text{-}CI}} = \langle \Psi_{m\to n}^{\mathrm{SAC\text{-}CI}} | H | \Psi_0^{\mathrm{SAC}} \rangle$$
$$= \sum_k d_k^* \langle \Psi_0^{\mathrm{HF}} | \exp\left(\sum_I C_I^* S_I \right) R_k H$$
$$\times \exp\left(\sum_J C_J S_J^+ \right) | \Psi_0^{\mathrm{HF}} \rangle. \quad (19)$$

Since the energies of the initial and final states are obtained using the CI or SAC/SAC-CI method, the energy difference in Eq. (7) is calculated directly, rather than the orbital energy difference $\epsilon_m - \epsilon_n$.

III. APPLICATION TO SIMPLE TIP–SAMPLE SYSTEMS

A. Model clusters

In this section, we apply our model of STM presented above to simple tip–sample systems such as Pd_2–Ag_2, Pd_2–C_6H_6, Pd_2–$(C_6H_6)_2$, and Li_2–Li_2. The tips are modeled by Pd_2 and Li_2, and the samples are modeled by Ag_2, C_6H_6, $(C_6H_6)_2$, and Li_2. As shown in Fig. 1, which depicts the geometrical structures of the model clusters, the tips are perpendicular to the sample surfaces. The distances between them are held constant throughout scanning, which corresponds to the experimental constant-height mode. The M–M (M=Pd, Ag, and Li) distances are fixed at the experimental lattice constants 2.7511, 2.8894, and 3.039 Å, respectively.[17] The geometrical parameters of benzene are fixed at experimental values.[18] For the benzene dimer, two C_6H_6 planes are parallel and separated by 3.0 Å.

The Gaussian basis sets used for palladium and silver are $(3s3p4d)/[3s2p2d]$ sets, and the Kr cores are replaced by the relativistic effective core potentials.[19] A diffuse s function of $\alpha=0.0066$ is adopted for Ag to examine the effect of the Rydberg orbital. For carbon and hydrogen, we use the $(9s5p)/[4s2p]$ and $(4s)/[2s]$ sets of Huzinaga–Dunning.[20,21] For the benzene dimer, we use STO-3G basis sets.[22] The 6-31G set is used for Li.[23] The HF and SAC/SAC-CI calculations are performed using HONDO8 (Ref. 24) and SAC85 (Ref. 25) software, respectively. The SD-CI calculations are performed using SAC85 software.

Simulated STM images are drawn for the Pd_2–Ag_2, Pd_2–C_6H_6, and Pd_2–$(C_6H_6)_2$ systems as contour maps of the transition matrices $|M_{m\to n}|^2$ calculated by the HF method. In this simulation, only a single-electron transition is taken into account for simplicity. However, considering the band structure of the bulk solid, the STM image should be simulated by mixing multiple transitions in this model.

B. Pd_2–Ag_2 system

First, we show STM images of the Pd_2–Ag_2 system calculated by the HF method. Figures 2(a), 2(b), and 2(c) show the contour maps of the tunneling matrix elements $|M_{m\to n}|^2$ for three kinds of tunneling transitions; i.e. (a) HOMO of Pd_2 to LUMO of Ag_2, (b) HOMO of Ag_2 to LUMO of Pd_2, and (c) next-HOMO of Pd_2 to LUMO of Ag_2.

There are two peaks in Fig. 2(a) near the Ag atoms, and $|M_{m\to n}|^2$ at the bisector of the Ag–Ag bond is zero. On the

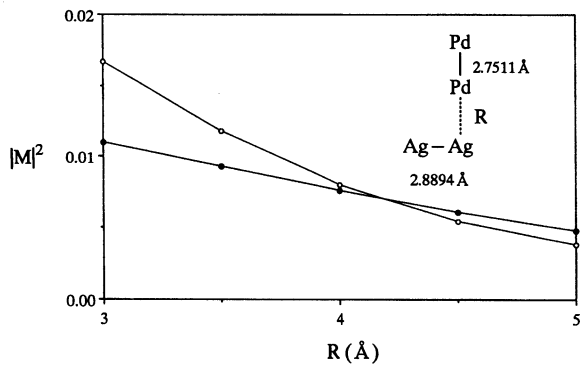

FIG. 3. Tip–sample distance-dependency of the tunneling transition probability $|M_{m\to n}|^2$ calculated for the Pd_2–Ag_2 system using two types of tunneling; one from the $4d\sigma^*$ HOMO of Pd_2 to the valence-type $5s\sigma^*$ LUMO of Ag_2 (white dots); one from the HOMO of Pd_2 to the Rydberg-type $6s\sigma^*$ next-LUMO of Ag_2 (black dots).

other hand, Fig. 2(b) shows a peak of $|M_{m\to n}|^2$ at the center of Ag_2. In this image, we observe the chemical bond of Ag_2 instead of the positions of the atomic nuclei. This difference is due to the characteristics of the orbitals observed by the tunneling; i.e., the LUMO of Ag_2, to which an electron transfers in Fig. 2(a), is the $5s\sigma^*$ MO which has a node at the center, while the HOMO of Ag_2, from which an electron transfers in Fig. 2(b), is the nodeless $5s\sigma$ MO. Since the Hamiltonian in Eq. (11) is totally symmetric, the tunneling matrix element between the orthogonal MOs is zero, which corresponds to the center line in Fig. 2(a). Note that the two peaks in Fig. 2(a) fall outside of the Ag atoms; mixing of the $5p_x$ orbitals with the LUMO of Ag_2 expands the robe.

Figure 2(c) corresponds to tunneling from the degenerate $4d\pi^*$ MOs of Pd_2 to the $5s\sigma^*$ MO of Ag_2. Since the two MOs are not orthogonal, even when Pd_2 is above the center of the Ag–Ag bond, the calculated values of $|M_{m\to n}|^2$ are always nonzero. This image has a peak at the center, which is similar to that in Fig. 2(b). However, in this image we observe the antibonding MO of Ag_2. The peak is not a simple circle, but is distorted, which shows that the electronic structure of the tip strongly influences the image.

We next examine the effect of the Rydberg orbital on the sample surface. As mentioned above, we add a diffuse s function of α=0.0066 as the $6s$ orbital of Ag. The tunneling matrix elements $|M_{m\to n}|^2$ are calculated at Pd–Ag distances of 3–5 Å, with the geometry of the Pd_2–Ag_2 system illustrated in Fig. 3. Two kinds of tunneling are examined, i.e., from the $4d\sigma^*$ MO of Pd_2 to the $5s\sigma^*$ MO and the $6s\sigma^*$ MO of Ag_2, the former being the valence-type vacant orbital and the latter the Rydberg-type vacant orbital.

The value of $|M_{m\to n}|^2$ for valence-type tunneling decreases exponentially as the Pd–Ag distance increases, which is consistent with various experimental findings. This is expected from the distance-dependence of the two-center overlapping integrals, and a similar result has been reported by Tersoff and Hamann.[2] This result also shows that the tunneling current reflects the local nature of the tip and the sample and supports that the top atom of the tip plays the most important role in the tunneling current.[5–7] This implies that metal dimers are not a bad model for the tip, though the tip-size dependence of the STM current would exist.

In contrast, the value of $|M_{m\to n}|^2$ for Rydberg-type tunneling decreases more gently as the Pd–Ag distance increases. This behavior reflects the diffuse nature of the Rydberg orbital. As seen in Fig. 3, the tunneling matrix element through the valence orbital is larger than that through the Rydberg orbital at shorter tip–sample distances. Therefore, these results indicate that scanning with shorter tip–sample distances should give a higher resolution than that using greater separations because of the rigidity of the valence-type vacant orbitals. When scanning is performed using larger tip–sample distances, it may become difficult to analyze the nature of the transitions because the Rydberg- and valence-type transitions may become comparable.

C. Pd_2–C_6H_6 system

Next, we calculate the Pd_2–C_6H_6 system using the HF method. Figures 4(a)–4(d) show the contour maps of the tunneling matrix element $|M_{m\to n}|^2$ for four kinds of tunneling transitions; i.e., (a) HOMO of Pd_2 to LUMOs of C_6H_6, (b) HOMO of C_6H_6 to LUMO of Pd_2, (c) next-HOMOs of Pd_2 to LUMOs of C_6H_6, and (d) two next-HOMOs of C_6H_6 to LUMOs of Pd_2.

Figure 4(a) shows six peaks corresponding to six carbon atoms. These peaks are due to the existence of nodes at the center of the C–C bonds, as in the Pd_2–Ag_2 system. The six peaks in Fig. 4(a) fall outside of the six carbon atoms. In this case, this may be due to interaction between AOs with phases that are different than the neighbor C atoms, since the lobes of the LUMOs of C_6H_6 are perpendicular to the C_6H_6 plane.

Figure 4(b) corresponds to tunneling from the degenerate HOMOs of C_6H_6 to the LUMOs of Pd_2. The image shows a doughnutlike ring, which is due to the scarcity of nodes in the HOMOs of C_6H_6 and the diffuse nature of the LUMOs of Pd_2 as compared to the C_6H_6 ring. The peak is placed outside of the carbon atoms for the same reason as in Fig. 4(a).

Figure 4(c) shows the six peaks above the bonds. These peaks appear just above the bonds, not outside the bonds as in Fig. 4(a). Since both the MOs of the tip and sample have nodes perpendicular to the C_6H_6 plane, the phases agree at the bond centers.

Figure 4(d) corresponds to tunneling from a nodeless a_{1g} orbital of C_6H_6 to the LUMOs of Pd_2. The image shows only one peak at the center of the C_6H_6 ring. This indicates that a C_6H_6 molecule appears as a single hemisphere.

Figure 4(a) shows some similarity to the experimental STM image of benzene adsorbed on a Rh(111) surface.[26] In this experiment, the electron flows from the tip to the sample at a low bias voltage, so that the STM image of benzene shows a dip at the center and three peaks outside of the benzene ring. This resembles Fig. 4(a), although the number of peaks does not agree with the experimental image, probably due to the effect of the Rh surface layer.

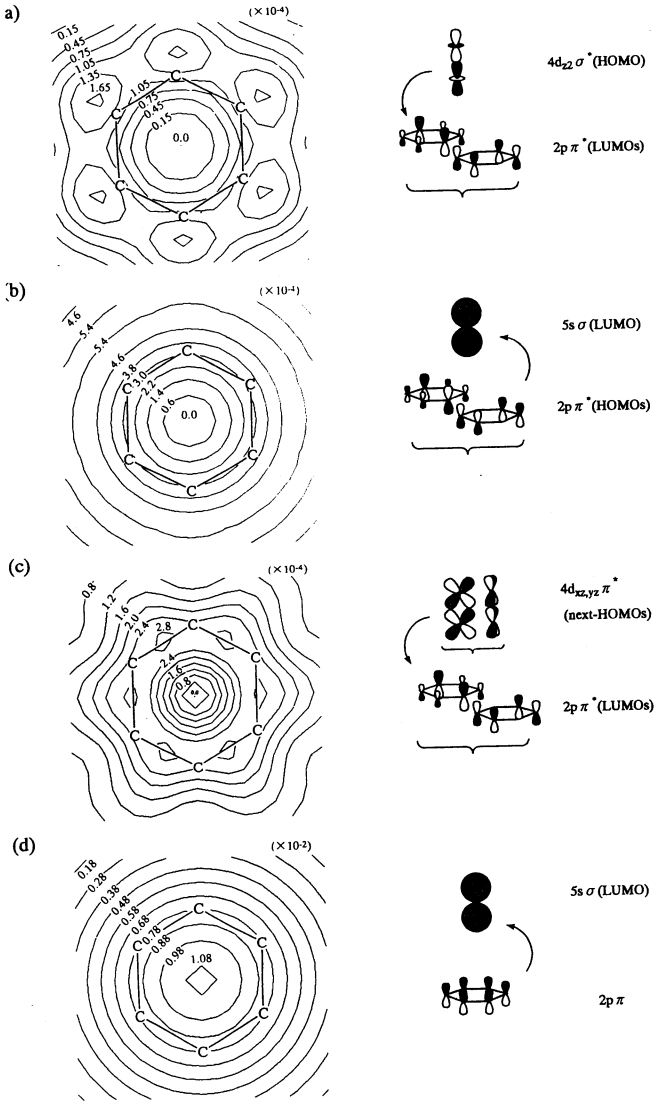

FIG. 4. Theoretical STM images of the variation of $|M_{m\to n}|^2$ for the Pd_2–C_6H_6 system with the geometrical structure shown in Fig. 1(b). The images are drawn as for the Pd_2–Ag_2 system in Fig. 2.

An analysis of the values of $|M_{m\to n}|^2$ in both the Pd_2–Ag_2 and Pd_2–C_6H_6 systems shows that tunnelings to the antibonding orbitals of the sample have smaller values of $|M_{m\to n}|^2$ than those to the bonding orbitals. This is likely caused by distant AOs with opposite phases.

D. Pd_2–$(C_6H_6)_2$ system

Albrecht *et al.* reported an experimental STM image of a graphite (0001) surface[27] shown in Figs. 5(a) and 5(b), where we see only triangular peaks instead of the hexagonal peaks of benzene rings. On the graphite (0001) surface, there exist two types of carbon atoms, α and β; the α-site carbon atoms have the carbon atoms just below them and the β-site carbon atoms do not.

We have tried to simulate the STM image of a graphite (0001) surface using $(C_6H_6)_2$ as a model of the first and second layers of graphite and compared the images of the α- and β-site carbon atoms [see Fig. 5(c)]. Since the HF calculation shows that there is an energy gap between the LUMO and the next LUMO of $(C_6H_6)_2$, which originate from the degenerate LUMOs of C_6H_6, we calculate $|M_{m\to n}|^2$ as a sum at a ratio of 1:0.9 from the HOMOs of Pd_2 to the LUMO and the next LUMO of $(C_6H_6)_2$. The calculated image shown in Fig. 5(c) indicates that the peak at the β carbon atom is larger than the peaks at the α carbon atoms. Previous theoretical studies[7,11] have shown similar results. Accordingly, the experimental STM image shows the triangular peaks corresponding to the three carbon atoms of the six benzene-ring carbon atoms. This is explained by the characteristics of the LUMO and the next LUMO of $(C_6H_6)_2$ shown in Fig. 6. Since the β-site carbon atom has a larger coefficient than the α-site one in the LUMO, a larger peak appears at the β site. The inequality between the α- and β-site carbon atoms caused by the interaction with the second layer leads to the peaks only at the β sites, that is, the peaks of every other carbon atoms of the graphite first layer.

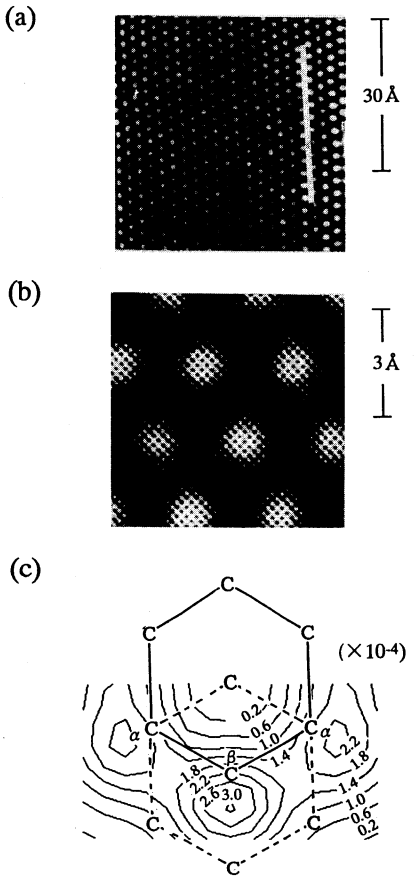

FIG. 5. (a) Experimental STM image of the graphite (0001) surface cited from Ref. 27. The peaks are arranged triangularly. The white line indicates the lattice orientation. (b) The enlarged image of (a). (c) Theoretical STM image of the Pd_2–$(C_6H_6)_2$ system using 1:0.9 sum of $|M_{m\to n}|^2$ of the tunnelings from the HOMOs of Pd_2 to the LUMO and the next-LUMO of $(C_6H_6)_2$.

E. Li_2–Li_2 system; electron correlations

Finally, we examine the effect of electron correlations on STM images using a Li_2–Li_2 system. The tunneling matrix

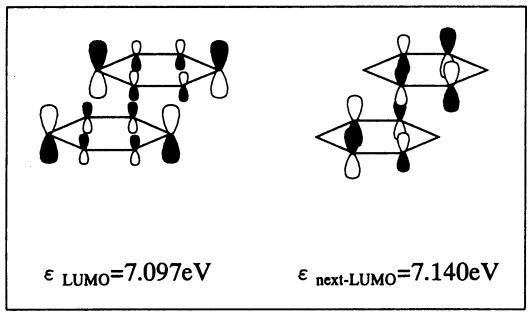

FIG. 6. Characteristics of the LUMO and the next-LUMO of $(C_6H_6)_2$. Their orbital energies are also shown. The β carbon atom has a larger coefficient than the α carbon atoms in the LUMO.

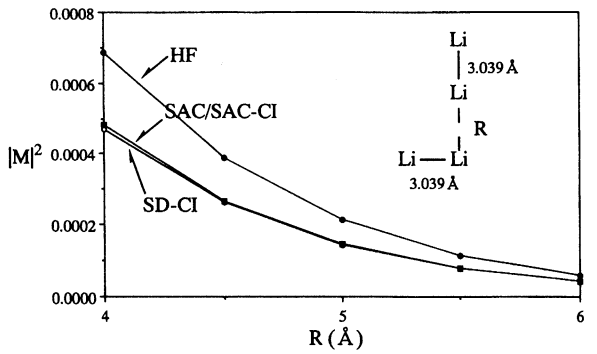

FIG. 8. Comparison of the tip–sample distance-dependency of $|M_{m\to n}|^2$ calculated by the HF, SD-CI, and SAC/SAC-CI methods.

elements $|M_{m\to n}|^2$ are calculated using Eqs. (16) and (18) from the SD-CI and SAC/SAC-CI wave functions, respectively. In the summation of Eq. (18), the unlinked parts of the SAC and SAC-CI wave functions representing more-than-three electron excitations are not included.

Figure 7 shows the contour maps of the tunneling matrix elements $|M_{m\to n}|^2$ calculated by the SD-CI and SAC/SAC-CI methods [Figs. 7(a), 7(b), 7(α), and 7(β)] and compares these with the HF results [Figs. 7(c) and 7(γ)]. The calculations are performed for the two-way lowest-energy transitions. The main configurations of the final states in the SD-CI and SAC/SAC-CI calculations are the charge-transferred ones; i.e., from the HOMO of the tip Li_2 to the LUMO of the sample Li_2, and from the HOMO of the sample to the LUMO of the tip.

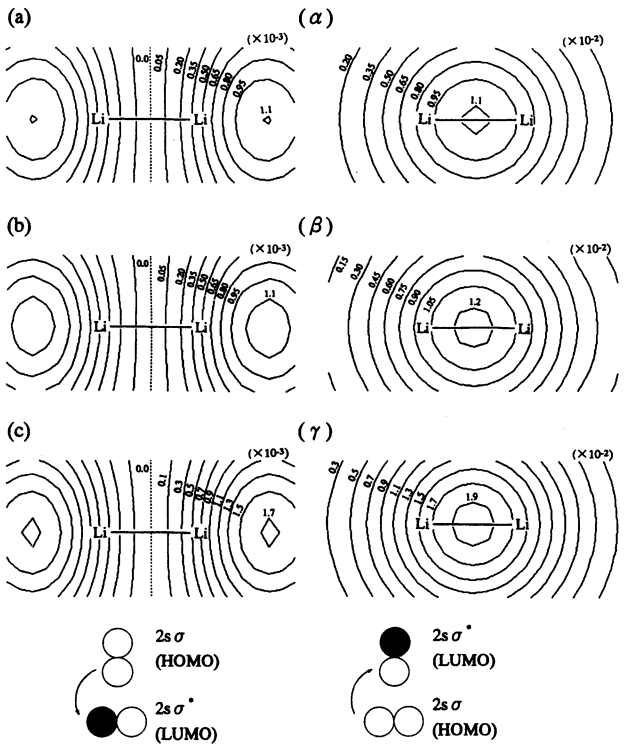

FIG. 7. Comparison of the theoretical STM images drawn using the SD-CI (a, α), SAC/SAC-CI (b, β), and HF (c, γ) methods for two-way HOMO-LUMO transitions (tip to sample; alphabetic notations, sample to tip; Greek notations) of the Li_2–Li_2 system in Tables I and II.

Figure 7 shows that the maps of the correlated methods have gentler slopes and smaller contour values than those of the HF method. The orthogonality on the center line normal to the bond in the case of the tip-to-sample transition is retained in the correlated calculation. The difference between the SD-CI and the SAC/SAC-CI methods is small because the Li_2–Li_2 system is likely little improved by considering the triple and quadruple excitation configuration in the SAC/SAC-CI calculation.

Figure 8 shows the distance-dependency of the transition from HOMO of the tip Li_2 to LUMO of the sample Li_2 using the HF and correlated methods. In all cases, the values of $|M_{m\to n}|^2$ decrease exponentially as the tip–sample distance increases. The two curves of the correlated methods are similar to each other and are located below that of the HF method.

IV. SUMMARY AND CONCLUSIONS

We have developed an *ab initio* model of STM. First, we applied the HF method to Bardeen's perturbative theory and formulated the tunneling transition probability $M_{m\to n}$, which is calculated analytically in the present method. Second, we obtained the correlated form of the tunneling transition probability using the CI and SAC/SAC-CI methods.

We also performed some calculations of the STM image using the HF method on simple tip–sample systems; Pd_2–Ag_2, Pd_2–C_6H_6, and Pd_2–$(C_6H_6)_2$. By doing so, we were able to offer some explanations for the inconsistency between STM images and actual atomic arrangements, and formulated some rules for determining the STM image, as shown in Fig. 9. When the tip's orbitals that are dominant to the tunneling have no nodes vertical to the sample plane, the STM image is easily analyzed. When the sample's orbitals are bonding and have no nodes, the STM image is independent of the atomic arrangement of the sample's orbitals, and sometimes shows peaks at positions where there are no atoms (case 1 in Fig. 9). When the sample's orbitals are antibonding and have many nodes, the STM image reasonably

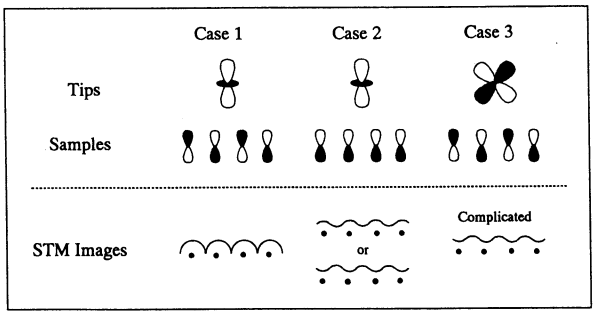

FIG. 9. Rules regarding STM images deduced from the present simulations. When the tip's orbitals have no nodes vertical to the sample plane and the sample's orbitals are bonding and have no nodes, the STM image is independent of the atomic arrangement of the sample's orbitals, and sometimes shows a peak where there are no atoms (case 1). When the sample's orbitals are antibonding and have many nodes, the STM image reasonably reflects the atomic arrangement of the sample's orbitals (case 2). When the tip's orbitals have nodes vertical to the sample plane, the STM image is too complicated for analysis (case 3).

reflects the atomic arrangement of the sample (case 2 in Fig. 9). When the tip's orbitals that are dominant to the tunneling have nodes vertical to the sample plane, the STM image is so complicated that it is difficult to understand what is actually being observed (case 3 in Fig. 9). The effect of the electronic state of the tip on the STM image is quite large, as demonstrated using previous models.

Based on these considerations, we expect that, to obtain a STM image that reflects the atomic arrangement, we should adjust the experimental conditions so that the tunneling current flows from the sample to the tip. This corresponds to flowing of the tunneling electrons from the occupied states of the tip, which would be smaller and have less nodes, to the vacant state of the sample, which would have more nodes. An explanation for why the STM image observed using a popular W tip has high resolution is that the d_z-type orbital is dominant to the tunneling. The effect of the Rydberg orbital was also examined for the Pd_2–Ag_2 system. We recommend that the STM image should be observed under conditions in which the valence-type transitions are dominant to obtain a high-resolution STM image.

Using the SD-CI and SAC/SAC-CI methods, we examined the effect of electron correlations for the first time in the Li_2–Li_2 system. We found that electron correlations work to decrease the values of $|M_{m\to n}|^2$ due to occupation of the antibonding MOs in the correlated wave functions. The tip–sample distance-dependency of $|M_{m\to n}|^2$ decreases due to the effect of electron correlations.

The many factors related to a STM tunneling current are expected to be very complicated. For example, although we considered a tunneling electron flowing from the occupied state of one conductor to the unoccupied state of another, if in fact the electron stays at the surface of one conductor temporarily before tunneling, then a tunneling electron would flow from the unoccupied state of one conductor to the unoccupied state of another.

ACKNOWLEDGMENT

Part of this study was supported by a Grant-in-Aid for Scientific Research from the Ministry of Education, Science, and Culture of Japan.

[1] G. Binnig, H. Rohrer, Ch. Gerber, and E. Weibel, Appl. Phys. Lett. **49**, 57 (1982); **50**, 120 (1983).
[2] J. Tersoff and D. R. Hamann, Phys. Rev. B **31**, 805 (1985); Phys. Rev. Lett. **50**, 1998 (1983).
[3] N. Garcia, C. Ocal, and F. Flores, Phys. Rev. Lett. **50**, 2002 (1983).
[4] N. D. Lang, Phys. Rev. Lett. **56**, 1164 (1986); **58**, 45 (1987).
[5] M. Tsukada and N. Shima, J. Phys. Soc. Jpn. **56**, 2875 (1987).
[6] M. Tsukada, K. Kobayshi, N. Isshiki, and Y. Hasegawa, Surf. Sci. Rep. **13**, 265 (1991).
[7] N. Isshiki, K. Kobayshi, and M. Tsukada, Surf. Sci. **238**, L439 (1990).
[8] E. Tekman and S. Ciraci, Phys. Rev. B **40**, 10 286 (1989).
[9] W. Sacks and C. Noguera, Phys. Rev. B **43**, 11 612 (1991).
[10] P. Sautet and C. Joachim, Chem. Phys. Lett. **185**, 23 (1991).
[11] H. Ou-Yang, B. Källebring, and R. A. Marcus, J. Chem. Phys. **98**, 7565 (1993).
[12] J. Bardeen, Phys. Rev. Lett. **6**, 57 (1961).
[13] J. R. Oppenheimer, Phys. Rev. **31**, 66 (1928).
[14] H. Nakatsuji and K. Hirao, J. Chem. Phys. **68**, 2053 (1978).
[15] H. Nakatsuji, Chem. Phys. Lett. **59**, 362 (1978); **67**, 329, 334 (1979).
[16] H. Nakatsuji, Acta Chim. Hung. Models in Chem. **120**, 719 (1992).
[17] *CRC Handbook of Chemistry and Physics*, 65th ed. (Chemical Rubber, Cleveland, 1984–1985).
[18] *Tables of Interatomic Distances and Configuration in Molecules and Ions*, Special Publication No. 18 (The Chemical Society, London, 1965).
[19] P. J. Hay and W. R. Wadt, J. Chem. Phys. **82**, 299 (1985).
[20] S. Huzinaga, J. Chem. Phys. **42**, 1293 (1965).
[21] T. H. Dunning, J. Chem. Phys. **53**, 2823 (1970).
[22] W. J. Hehre, R. F. Stewart, and J. A. Pople, J. Chem. Phys. **51**, 2657 (1969).
[23] R. Ditchfield, W. J. Hehre, and J. A. Pople, J. Chem. Phys. **54**, 724 (1971).
[24] M. Dupuis and A. Farazdel, A. MOTECC-91, Center for Scientific and Engineering Computations, IBM Corporation, 1991.
[25] H. Nakatsuji, program system for SAC and SAC-CI calculations, Program Library No. 146 (Y4/SAC), Data Processing Center of Kyoto University, 1985; Program Library SAC85, No. 1396, Computer Center of the Institute for Molecular Science, 1981.
[26] H. Ohtani, R. J. Wilson, S. Chiang, and C. M. Mate, Phys. Rev. Lett. **60**, 2398 (1988).
[27] T. R. Albrecht, H. A. Mizes, J. Nogami, Sang-il Park, and C. F. Quate, Appl. Phys. Lett. **52**, 362 (1988).